Conjugated Foldamers with Unusually High Space-Charge-Limited Current Hole Mobilities

Yong Li,[†] Tanmoy Dutta,[†] Nikolay Gerasimchuk,[§] Shijie Wu,[‖] Kuldeep Shetye,[†] Lu Jin,[†] Ruixin Wang,[†] Da-Ming Zhu,[‡] and Zhonghua Peng*,[†]

[†]Department of Chemistry and [‡]Department of Physics, University of Missouri-Kansas City, Kansas City, Missouri 64110, United States

[§]Department of Chemistry, Missouri State University, Springfield, Missouri 65897, United States

[‖]Nano Scale Sciences Division, Keysight Technologies, Inc., Santa Clara, California 95051, United States

S *Supporting Information*

ABSTRACT: Charge carrier mobility and its optimization play a critical role in the development of cutting-edge organic electronic and optoelectronic devices. Even though space-charge-limited current (SCLC) hole mobilities as high as 1.4 $cm^2 V^{-1} s^{-1}$ have been reported for microscopically sized highly ordered liquid-crystalline conjugated small molecules, the SCLC hole mobility of device-sized thin films of conjugated polymers is still much lower, ranging from 10^{-6} to 10^{-3} $cm^2 V^{-1} s^{-1}$. Herein, we report the synthesis, characterizations, and thin-film SCLC mobility of three discotic conjugated polymers,

μ_h (SCLC):
0.129 $cm^2 V^{-1} s^{-1}$

Top-View   Side-View

INDT-TT, **INDT-BT**, and **INDT-NDT**. Optical studies indicate that polymer **INDT-NDT** adopts a folded conformation in solutions of good or poor solvents, whereas polymer **INDT-TT** stays as random monomeric chains in good solvents and interchain aggregates in poor solvents. **INDT-BT** polymer chains, however, stay as foldamers in dilute solutions of good solvents but interchain aggregates in concentrated solutions or poor solvents. Circular dichroism spectroscopy provides clear evidence for the helical folding of **INDT-NDT** in solutions. Thin films spin-coated from 1,2-dichlorobenzene solutions of the polymers show SCLC hole mobility of 2.20×10^{-6}, 8.79×10^{-5}, and 2.77×10^{-2} $cm^2 V^{-1} s^{-1}$ for **INDT-TT**, **INDT-BT**, and **INDT-NDT**, respectively. HRTEM and powder XRD measurements show that **INDT-NDT** pristine thin films contain nanocrystalline domains, whereas the **INDT-TT** and **INDT-BT** films are amorphous. Thin films of **INDT-NDT**:PC$_{71}$BM blends show increased crystallinity and further improved SCLC hole mobility up to 1.29×10^{-1} $cm^2 V^{-1} s^{-1}$, one of the highest SCLC mobility values ever recorded on solution-processed organic semiconducting thin films. The persistent folding conformation of **INDT-NDT** is believed to be responsible for the high crystallinity of its thin films and its high SCLC mobilities.

KEYWORDS: *conjugated polymers, conjugated foldamers, circular dichroism, helical bias, hole mobility, space-charge-limited current*
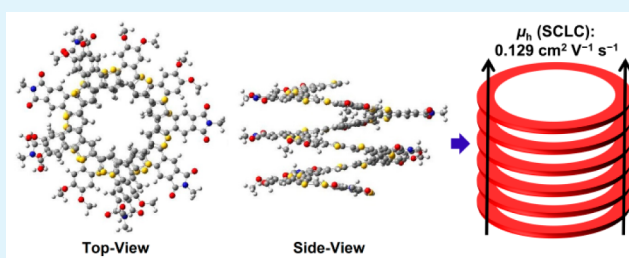
INTRODUCTION

Charge carrier mobility is one of the crucial parameters determining the performance of many organic electronic and optoelectronic devices.[1,2] The charge carrier mobility of an organic semiconductor depends not only on its molecular structure but also on the intermolecular interactions that are affected by morphology, packing order, and orientation.[3−6] Charge carrier mobility of conjugated polymers can be measured by a variety of techniques, among which the field-effect transistor (FET) method and the space-charge-limited current (SCLC) method are the most widely used. The FET method measures the mobility parallel to the electrodes under the influence of a gate bias, whereas the SCLC method measures the mobility perpendicular to the electrodes; both find important applications in electronics and optoelectronics.[7−9] FET hole mobilities in excess of 0.1 $cm^2 V^{-1} s^{-1}$ and up to 12 $cm^2 V^{-1} s^{-1}$ are well-known in solution-processed thin films of conjugated polymers;[4,10,11] the SCLC hole

mobilities of solution-processed thin films of conjugated polymers are however often lower by a few orders of magnitude,[8,12−14] typically ranging from 10^{-6} to 10^{-3} $cm^2 V^{-1} s^{-1}$ with only a couple of very recent reports of SCLC hole mobilities up to 2.3×10^{-2} $cm^2 V^{-1} s^{-1}$.[15,16] The generally low SCLC hole mobilities in solution-processed thin films of conjugated polymers are often due to their amorphous film morphology that lacks long-range ordered structures essential for efficient charge transport.[4]

Among the myriad of conjugated polymers, those containing discotic polycyclic aromatic hydrocarbon (PAH) building blocks have drawn particular attention in the exploration of high charge carrier mobility materials.[17−24] The inclusion of planar or near-planar PAHs in the backbone results in an

Scheme 1. Synthesis of INDT-Containing Discotic Conjugated Polymers
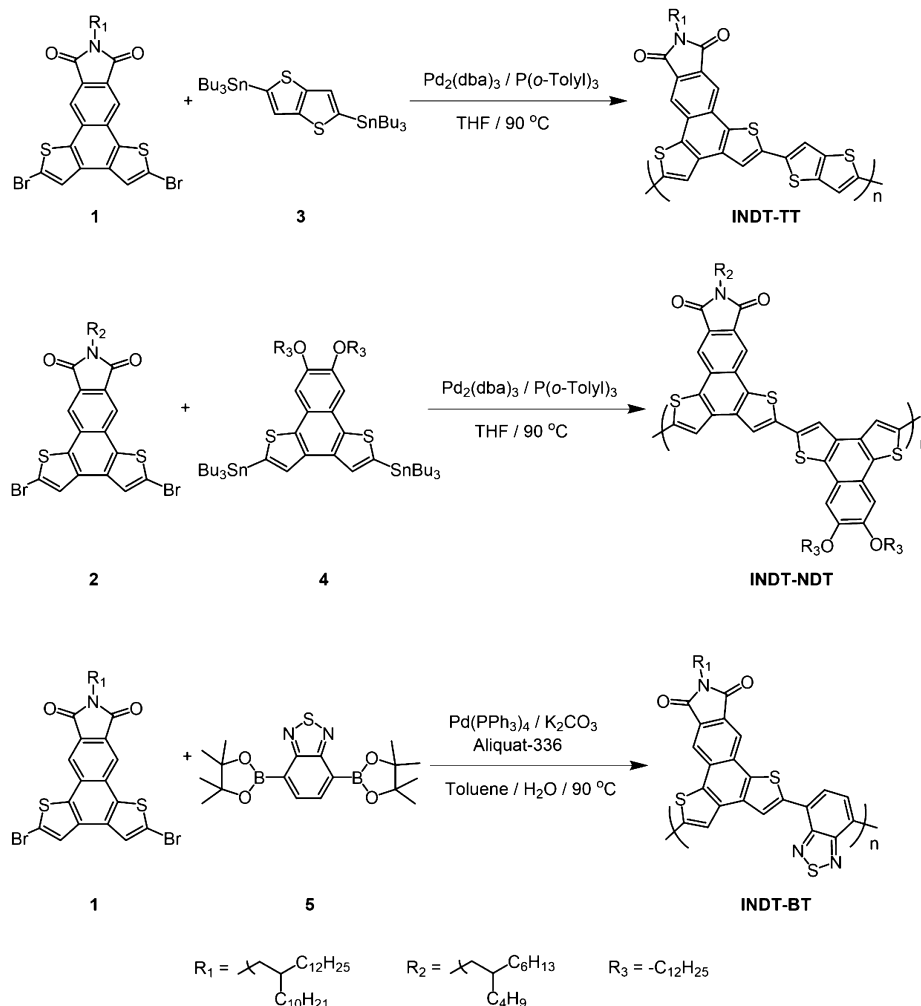
extended π-conjugated system in which forced planarity ensures stronger intermolecular π−π stacking interactions and induces potentially high charge carrier mobility along the backbone as well as the stacked PAH columns.[25−29] We have recently shown that a PAH-based imide-functionalized naphtho[1,2-*b*:4,3-*b'*]dithiophene (INDT) building block can be used to prepare low-bandgap donor−acceptor (D−A) conjugated polymers using substituted bithiophenes as the D unit.[30] Changing the backbone geometry via careful selection of the D unit can make it possible to synthesize INDT-based conjugated polymers with favorable bending angles that allow for the formation of helical foldamers. It is envisioned that with INDT (or other PAH building blocks) in the conjugated polymer backbone the polymer will not only exhibit strong propensity for folding virtually because of their strong stacking interactions but also may lead to conjugated foldamers with high charge mobilities. It is known that π-stacked columns formed from some PAHs exhibit strong electron delocalization among and high charge mobility through the stacked columns.[25−29] Foldamers based on PAH-containing conjugated polymers that form multiple PAH-stacked columns after folding may thus exhibit efficient charge-transporting properties.

In this work, we report three new INDT-containing conjugated polymers, namely, **INDT-TT**, **INDT-BT**, and **INDT-NDT**, with thienothiophene (TT), benzo[c]-1,2,5-thiadiazole (BT), and 8,9-bis(dodecyloxy)naphtho[1,2-*b*:4,3-*b'*]dithiophene (NDT) as the comonomer, respectively. It was found that these three polymers adopt very different conformations in solutions. In dilute solutions of a good solvent, **INDT-TT** polymers stay as monomeric random coils, whereas **INDT-BT** and **INDT-NDT** adopt the folding conformation. In concentrated solutions of a good solvent or solutions of a poor solvent, interchain aggregation dominates in **INDT-TT** and **INDT-BT**, whereas **INDT-NDT** maintains the folding conformation. Circular dichroism (CD) spectroscopy gave clear evidence for the helical folding of **INDT-NDT** polymer in solutions. Spin-coated thin films of **INDT-NDT** show nanocrystalline order and unusually high SCLC hole mobility, up to 2.77×10^{-2} cm^2 V^{-1} s^{-1}. After blending with PC$_{71}$BM, the film crystallinity is further improved, leading to one of the highest SCLC hole mobilities (1.29×10^{-1} cm^2 V^{-1} s^{-1}) in solution-processed organic semiconducting thin films. The persistent folding conformation of the **INDT-NDT** is believed to be responsible for the high crystallinity of its thin films and its high SCLC mobilities.

■ EXPERIMENTAL SECTION

General. Solvents were freshly distilled from appropriate drying agents under inert atmosphere prior to use. Unless otherwise noted, all other reagents were used as received from Fisher Scientific or Sigma-Aldrich without further purification. Highly conductive poly(3,4-ethylenedioxythiophene):poly(styrenesulfonate) (PEDOT:PSS, Cle-

vios P VP AI4083) was purchased from Heraeus Precious Metals. [6,6]-Phenyl-C_{71}-butyric acid methyl ester ($PC_{71}BM$), mixture of isomers, was purchased from Nano-C, Inc. Indium tin oxide (ITO)-coated glass with sheet resistance of 8–12 Ω/square was purchased from Delta Technologies. ^1H and ^{13}C NMR spectra were recorded on a Varian INOVA 400 MHz FTNMR spectrometer in deuterated solvents. Spectra were referenced internally to the residual solvent resonances. Gel permeation chromatography (GPC) data were collected at 30 °C using a Tosoh EcoSEC HLC-8320GPC system equipped with a refractive index (RI) detector, a UV detector, a light-scattering detector, and a styragel column. THF was used as the eluent. The instrument was calibrated by polystyrene standards. UV–vis absorption spectra were measured on a Hewlett-Packard 8452A diode array spectrophotometer. Fluorescence spectra were recorded with a Shimadzu RF-5301PC spectrofluorophotometer. Fluorescence quantum yields were determined in dilute solutions (absorption maximum < 0.1) using quinine sulfate in 1 N H_2SO_4 ($\varphi_{fl} \approx 0.546$) as the standard. CD spectra were recorded on a Jasco J-815 CD spectrometer using 1 cm quartz cells. Particle size data were collected on a Brookhaven NanoBrook Omni particle size analyzer using 1 cm quartz cells. Atomic force microscopy (AFM) images were taken in air under ambient conditions using the contact mode or Acoustic AC (AAC) mode on an atomic force microscope (Molecular Imaging Corporation or Keysight Technologies, Inc.). HRTEM images were taken with an FEI TECNAI F20 200 kV super-twin lens transmission electron microscope. Crystal structure characterization of the thin films coated on Si zero-diffraction plates was carried out by X-ray diffraction measurements with a Rigaku Miniflex automated powder X-ray diffractometer (Cu $K\alpha$, 35 kV, 15 mA, Ni filter, λ = 1.54178 Å).

Cyclic voltammetry (CV) studies of polymer thin films were carried out under argon atmosphere using a BAS Epsilon EC electrochemical station employing a Pt working electrode (MF-2013) of 1.6 mm in diameter, a silver wire as the reference electrode, and a Pt wire as the counter electrode. A drop of polymer solution (~1 mg mL^{-1}, in THF) was spread on the bare surface of the Pt working electrode and slowly dried in air. This procedure was repeated if necessary until a uniform thin film (judged by sight) was achieved. A 0.1 M tetra-n-butylammonium hexafluorophosphate solution in acetonitrile was used as supporting electrolyte, and the scan rate was 20 mV s^{-1}. The potentials were calibrated using a ferrocene/ferrocenium (Fc/Fc^+) redox couple. The highest occupied molecular orbital (HOMO) and the lowest unoccupied molecular orbital (LUMO) energy levels were calculated by the equations HOMO = $-(E_{ox}^{onset}$ + 4.80) eV and LUMO = $-(E_{red}^{onset}$ + 4.80) eV, respectively.[31]

Synthesis. Scheme 1 shows the synthesis of the three new conjugated polymers. Compounds **1** and **2** were prepared according to previously published procedures.[30] 2,5-Bis(tributylstannyl)thieno[3,2-b]thiophene (**3**) was synthesized from commercially available thieno[3,2-b]thiophene (Supporting Information). Compound **4** was synthesized from 2,5-dibromo-8,9-bis(dodecyloxy)naphtho[1,2-b:4,3-b']dithiophene (Supporting Information).[32] 2,1,3-Benzothiadiazole-4,7-bis(boronic acid pinacol ester) (**5**) was purchased from commercial sources.

Polymer INDT-TT. To an air-free flask were added **1** (100 mg, 0.12 mmol), **3** (90 mg, 0.12 mmol), $Pd_2(dba)_3$ (6 mg, 0.006 mmol), and P(o-Tolyl)$_3$ (15 mg, 0.05 mmol). The flask was subjected to three pump–purge cycles with argon followed by the addition of freshly distilled THF (5 mL) via syringe. The reaction flask was sealed and stirred at 90 °C for 48 h. After cooling to room temperature, the reaction mixture was poured into a solvent mixture containing 50 mL of methanol and 5 mL of 12 N HCl and stirred for 4 h. The precipitates were collected by centrifugation and redissolved in THF. After filtration to remove any insoluble component, the filtrate was again poured into methanol. The polymer precipitates were collected, dried under reduced pressure, and further purified by sequential Soxhlet extraction with methanol, acetone, and hexane. The residual polymer was finally extracted with chloroform. The chloroform solution was concentrated to 15 mL and precipitated into 100 mL of methanol. The polymer was isolated by centrifugation and dried under reduced pressure to yield a red solid (83 mg, 85%). ^1H NMR (400

MHz, $C_2D_2Cl_4$) δ/ppm 9.0–6.5 (extremely br, 6H, naphthodithiophene and comonomer aromatic H's), 4.2–3.0 (br, 2H, N–CH_2–), 2.5–0.5 (br, 47H, aliphatic H's). Molecular weights from GPC measurements: M_n = 11.6 kDa, M_w = 19.7 kDa, PDI = 1.7.

Polymer INDT-NDT. Polymer **INDT-NDT** was synthesized using a procedure similar to that of **INDT-TT** except for the workup procedures as described below. After cooling to room temperature, the reaction mixture was poured into a solvent mixture containing 50 mL of methanol and 5 mL of 12 N HCl and stirred for 4 h. The precipitates were collected by centrifugation and redissolved in chlorobenzene at an elevated temperature. After filtration to remove any insoluble component, the filtrate was again poured into methanol. The polymer precipitates were isolated by centrifugation and dried under reduced pressure to yield a dark yellow solid. Yield: 71%. ^1H NMR (400 MHz, $C_2D_2Cl_4$, 75 °C) δ/ppm 2.5–0.5 (extremely br, 69H, aliphatic H's). Molecular weights from GPC measurements (THF soluble part at room temperature): M_n = 7.1 kDa, M_w = 24.3 kDa, PDI = 3.4.

Polymer INDT-BT. To an air-free flask were added **1** (100 mg, 0.12 mmol), **5** (48 mg, 0.12 mmol), $Pd(PPh_3)_4$ (7 mg, 0.006 mmol), and Aliquat 336 (5 mg, 0.01 mmol). The flask was subjected to three pump–purge cycles with argon followed by addition of dry, oxygen-free toluene (5 mL) and degassed aqueous K_2CO_3 (2 mL, 2 M) via syringe. The reaction tube was sealed and stirred at 90 °C for 72 h. After cooling to room temperature, the reaction mixture was diluted with chloroform (60 mL). The chloroform solution was washed with brine (2 × 30 mL). After drying over $MgSO_4$, the reaction mixture was concentrated to 15 mL and then poured into 100 mL of methanol. The polymer precipitates were collected, dried under reduced pressure, and further purified by sequential Soxhlet extraction with methanol and acetone. The residual polymer was finally extracted with chloroform. The chloroform solution was concentrated to 15 mL and precipitated into 100 mL of methanol. The polymer was isolated by centrifugation and dried under reduced pressure to yield a red solid (90 mg, 93%). ^1H NMR (400 MHz, $C_2D_2Cl_4$) δ/ppm 9.0–6.5 (br, 6H, naphthodithiophene and comonomer aromatic H's), 4.2–3.0 (br, 2H, N–CH_2–), 2.5–0.5 (br, 47H, aliphatic H's). Molecular weights from GPC measurements: M_n = 10.4 kDa, M_w = 16.4 kDa, PDI = 1.6.

Device Fabrication and Characterization. ITO-coated glass slides were used as the substrates. Under the protection of Magic tape, the ITO films were patterned by etching with aqua regia vapor. The patterned ITO-coated glass substrates were cleaned in an ultrasonic bath sequentially by hot detergent, water, deionized water, toluene, acetone, and isopropyl alcohol and then dried by compressed air. The cleaned ITO substrates were treated with UV ozone for 45 min before use. A PEDOT:PSS thin layer was spin-coated (4000 rpm, 30 s) onto the ITO substrates from an aqueous solution. The PEDOT:PSS thin films were dried at 120 °C for 45 min on a hot plate in air. Polymer or polymer:$PC_{71}BM$ (1:1, w/w) blend solutions were prepared in a glovebox in nitrogen-degassed 1,2-dichlorobenzene (ODCB) with a polymer concentration of 20 mg mL^{-1}. The solutions were heated overnight at 50 °C with stirring, passed through a 0.45 μm filter, and spin-coated (1200 rpm, 1 min) on top of the PEDOT:PSS thin films. Solvent annealing was then performed by covering the wet films with a Petri dish for at least 45 min. The devices were dried in a nitrogen atmosphere under reduced pressure. Half of the films were thermally annealed at 120 °C for 10 min on a hot plate in the dark. Subsequently, through a shadow mask, electrodes composed of 10 nm thick MoO_3 and 100 nm thick Au were deposited on the top by thermal evaporation under high vacuum (<2 × 10^{-6} mbar). The active area of 0.14 cm^2 of the devices was defined by the overlap area of the ITO and the deposited MoO_3/Au electrodes. Current–voltage characteristics of the devices were measured using a Keithley 2400 source meter in the dark. The thickness of the films was measured with a Tencor Alphastep 200 automatic step profiler.

■ RESULTS AND DISCUSSION

The synthesis of the three INDT-containing conjugated polymers was depicted in Scheme 1. Polymers **INDT-TT** and
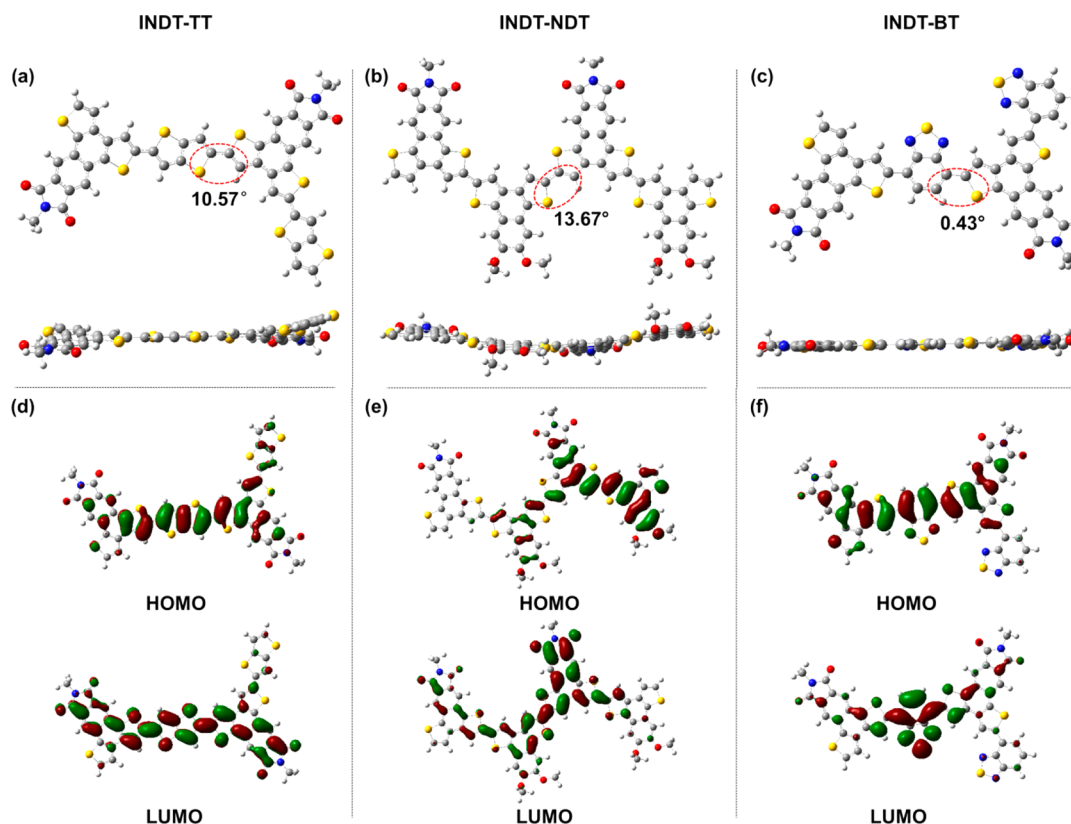
Figure 1. (a−c) Energy-minimized geometries from different views and (d−f) visualized HOMO/LUMO orbitals of **INDT-TT** (a and d), **INDT-NDT** (b and e), and **INDT-BT** (c and f) dimers obtained using DFT calculations at the B3LYP/6-31G(d) level.

INDT-NDT were synthesized using the Stille polycondensation reaction,[33] whereas polymer **INDT-BT** was synthesized using the Suzuki cross-coupling polymerization reaction with Aliquat-336 as a phase-transfer catalyst in a toluene/water solvent mixture.[34] With a long, branched 2-decyltetradecyl chain at the imide nitrogen position of INDT, polymers **INDT-TT** and **INDT-BT** exhibit good solubility in common organic solvents such as chloroform, THF, and toluene at room temperature. With more fused units in the backbone, polymer **INDT-NDT** is only partially soluble in these solvents at room temperature, even though there are two dodecyloxy groups attached to the NDT unit and a branched 2-butyloctyl group at the imide position of INDT.

Molecular weights of the three polymers were estimated by GPC with THF as the eluent and polystyrene as standards. For polymers **INDT-TT** and **INDT-BT**, the weight-average molecular weight (M_w) was found to be 20 and 16 kDa, respectively. Both polymers showed relatively narrow polydispersity indices (PDI = 1.7 and 1.6, respectively). Because of the limited solubility of **INDT-NDT**, only the soluble part was analyzed by GPC, and the M_w and PDI were found to be 24 kDa and 3.4, respectively.

The ^{1}H NMR spectra of the three polymers were measured using deuterated 1,1,2,2-tetrachloroethane as the solvent. Their aggregation properties were further studied using variable temperature (VT) ^{1}H NMR experiments. The ^{1}H NMR spectra of INDT monomer 1 shows two sharp singlets in the aromatic region at around 8.40 and 7.66 ppm, which can be assigned to the phenyl proton and the thiophene's β proton, respectively (signals a and b in Figure S1a). The TT-based comonomer 3 shows a singlet at 7.21 ppm (signal d in Figure S1b). After polymerization (**INDT-TT**), these proton signals become

extremely broad (Figure S1c), where the entire aromatic region shows one broad featureless hump. Even at a higher temperature (75 °C), the spectrum shows the same broad signals (Figure S2). The polymer **INDT-NDT** has two PAH-based monomer units in its backbone. The polymer lacks sufficient solubility at room temperature, so its ^{1}H NMR spectrum was recorded at a higher temperature (75 °C). Other than the clear broad aliphatic signals in the 0.9−2.0 ppm region, the ^{1}H NMR spectrum of **INDT-NDT** shows no peaks in the aromatic area. A small featureless broad hump between 3.0 and 4.5 ppm can be barely identified, which is attributed to −OCH$_2$ and N−CH$_2$− protons (Figure S3). The ^{1}H NMR spectrum of polymer **INDT-BT** shows signals with broadness similar to that of polymer **INDT-TT**. The aromatic region gave featureless broad bands (Figure S4), which became slightly resolved at a higher temperature (Figure S5). The exceedingly broad NMR spectra indicate that all three polymers have rather strong π-stacking interaction in concentrated solutions.

To help understand the backbone geometries and the electronic structures of the conjugated polymers, theoretical calculations were performed on their corresponding dimers using the density functional theory (DFT) with the Gaussian03 program[35] at the B3LYP level with the 6-31G(d) basis set.[36−40] To minimize the computational efforts, the alkyl chains at the imide position of INDTs, and the dodecyloxy chains in **INDT-NDT** were truncated to methyl and methoxy groups, respectively. Figure 1a−c shows the energy-minimized conformers of the three dimers from different views. Because of the fused nature of the comonomers (TT, NDT, and BT), only the twist between the comonomer and INDT is responsible for the backbone nonplanarity of these polymers. The dihedral angle between INDT and the adjacent comonomer is 10.57, 0.43, and

13.67° for **INDT-TT**, **INDT-BT**, and **INDT-NDT**, respectively. The significantly smaller dihedral angle in **INDT-BT** is presumably due to the unconventional hydrogen bonding between the basic N in the BT unit and the β H of thiophene, whose distance is calculated to be 2.30 Å.

The HOMO/LUMO energy levels and the bandgaps of the three polymers were estimated from the energy minimized conformers of their dimers. Figure 1d−f depicts the visualized HOMO and LUMO orbitals of the energy-minimized conformers. The HOMO/LUMO energy levels are found to be −5.44/−2.64, −5.36/−2.39, and −5.66/−3.16 eV for the dimers of **INDT-TT**, **INDT-NDT**, and **INDT-BT**, respectively, from which their bandgaps are calculated to be 2.80, 2.97, and 2.60 eV, respectively. It is worth noting that in the LUMO distribution of dimers of **INDT-TT** and **INDT-NDT** the node passes through the imide N atom, whereas the LUMO of **INDT-BT** dimer is concentrated on the BT unit and associated with a deeper energy level. It is evident that TT and NDT act as donor units in **INDT-TT** and **INDT-NDT**, whereas BT acts as an acceptor in **INDT-BT**.

The absorption spectra of the three polymers in dilute chloroform solutions are shown in Figure 2. Polymer **INDT-**
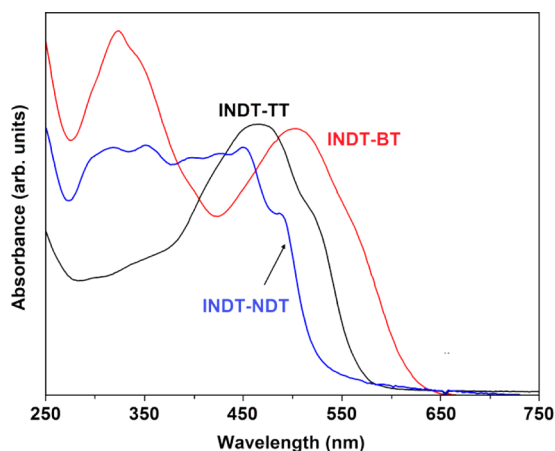
Figure 2. UV−vis absorption spectra of the three INDT-containing conjugated polymers in dilute chloroform solutions.

TT shows a major peak at 466 nm with a shoulder at ∼520 nm, whereas polymer **INDT-BT** gives two absorption bands at 324 and 504 nm with a shoulder at ∼560 nm. Polymer **INDT-NDT**, however, shows a broad absorption plateau ranging from 275 to 475 nm, with a shoulder peak at 490 nm. Both the absorption maxima (λ_{max}^{abs}) and the band edge shift to longer wavelengths from **INDT-NDT** to **INDT-TT** to **INDT-BT**. On the basis of the solution absorption spectra, the optical bandgaps were estimated to be 2.33, 2.12, and 2.00 eV, for **INDT-NDT**, **INDT-TT**, and **INDT-BT**, respectively.

All three polymers are weakly fluorescent in dilute solutions. (See fluorescence quantum yields in Table 1.) As shown in Figure 3, when excited at 466 nm (λ_{max}^{abs}) in chloroform, **INDT-**
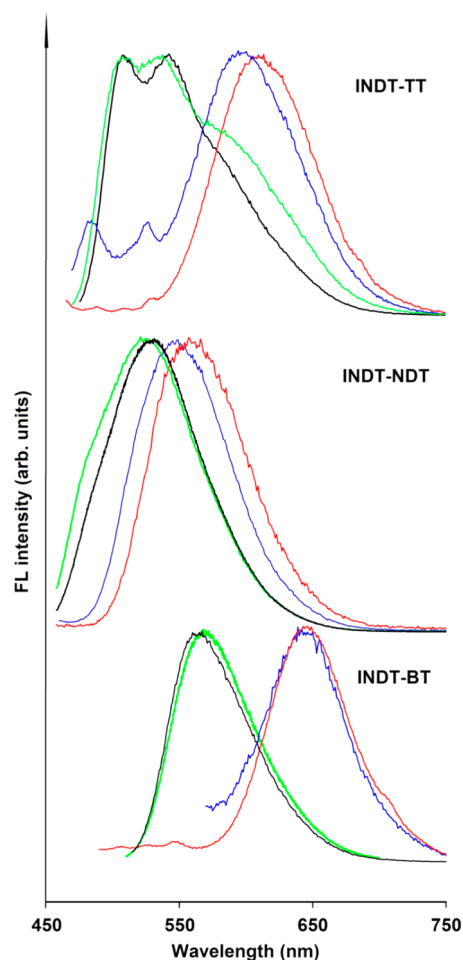
Figure 3. Fluorescence emission spectra of **INDT-TT**, **INDT-NDT**, and **INDT-BT** in dilute solutions of chloroform (black), THF (green), hexane (blue), and acetonitrile (red).

TT gives two emission bands at 510 and 540 nm, along with a shoulder at ∼580 nm. Excitation spectra measured at 510 and 540 nm emission wavelengths match each other very well (Figure S6), indicating that the 510 and 540 nm emission bands come from the same exciton. When excited at 520 nm (the shoulder band in its absorption spectra), only one major emission peak at 580 nm is observed (Figure S7). In acetonitrile, a poor solvent for **INDT-TT**, a broad structureless emission with a peak wavelength at 610 nm is observed, which is independent of the excitation wavelengths. These results clearly indicate that the 580/610 nm emission and the 510/540 nm emission bands are due to different excitons. The

Table 1. Optical Properties of the Polymers in Dilute Solutions

polymer	λ_{max}^{abs} (nm)[a]	λ_{max}^{fl} (nm)[a]	E_g^{opt} (eV)[b]	ϕ_{fl}			
				CHCl₃	THF	hexane	acetonitrile
INDT-TT	466	510, 540	2.12	0.013	0.014	0.010	0.002
INDT-NDT[c]	275−475[d]	530	2.33	0.039	0.052	0.015	0.009
INDT-BT	324, 504	560	2.00	0.032	0.025	0.006	<0.001

[a]In CHCl₃. [b]Optical bandgap was estimated from UV−vis absorption onset by $E_g^{opt} = 1240/\lambda_{onset}^{abs}$ (eV). [c]Soluble part of the polymer. [d]Broad peak.

Figure 4. Changes in fluorescence emission spectra of freshly prepared CHCl$_3$ solutions of (a) **INDT-TT** (c_0 = 0.245 mM; λ_{ex} = 466 nm), (b) **INDT-NDT** ($c_0{}'$ = 0.471 mM; λ_{ex} = 450 nm), and (c) **INDT-BT** ($c_0{}''$ = 0.694 mM; λ_{ex} = 504 nm) upon continuous dilution. For clarity, selected curves are rescaled.

vibronically resolved 510/540 nm emissions are likely from singlet excitons associated with **INDT-TT** in a random-coil nonaggregated conformation, whereas the broad structureless emission at 580/610 nm is presumably due to excimer/exciplex emissions resulting from interchain aggregation.

Unlike **INDT-TT**, which shows vibronically resolved emissions in good solvents (for example, chloroform and THF), **INDT-NDT** and **INDT-BT** show broad structureless emissions in both good and poor solvents, even at extremely dilute conditions. As shown in Figure 3, the emission λ_{max} of **INDT-NDT** in chloroform is 530 nm, which is red-shifted by 20 nm over the monomeric emission of **INDT-TT** even though the absorption λ_{max} and band edge of **INDT-NDT** are lower than those of **INDT-TT**. These results not only corroborate with the ^{1}H NMR data showing that **INDT-NDT** is highly aggregated but also indicate that it is through intrachain aggregation. We suggest that such an aggregation is driven by the strong $\pi-\pi$ interaction among stacked PAH rings (Figure S8). Intrapolymer self-aggregation results in helical polymer chains and leads to stacked PAH columns. It is known that charge transport through stacked discotic liquid-crystal columns can be quite efficient.[25-28] It is intriguing and interesting to see how efficient **INDT-NDT** polymer transports charges, which is discussed later.

INDT-BT in chloroform also shows a broad emission band without vibronic structures, indicating that **INDT-BT** in chloroform may adopt a folded conformation as well.[41] When the solvent is changed from chloroform to acetonitrile, a poor solvent for both **INDT-NDT** and **INDT-BT**, broad red-shifted emissions are again observed for both polymers. However, the extent of redshift is significantly different for the two polymers. Although **INDT-NDT** sees a redshift in emission λ_{max} of only about 30 nm, **INDT-BT** shows a shift of 85 nm. It is likely that in a poor solvent interchain $\pi-\pi$ stacking dominates for **INDT-BT** but intrachain folding dominates for **INDT-NDT**. The strong interchain stacking of **INDT-BT** may be due to its much smaller twist between comonomers and thus much flatter polymer backbone. This interpretation is supported by observations made from more extensive solvent dependent studies of their fluorescence properties. As shown in Figure 3, which shows the emission spectra of polymers in THF, chloroform, hexane, and acetonitrile, the emissions of **INDT-BT** broke into two well-separated groups: λ_{max} is around 560 nm in good solvents (chloroform and THF) and 645 nm in poor solvents (hexane and acetonitrile). **INDT-NDT**, however, shows small but continuously red-shifted emissions from THF

(525 nm) to CHCl$_3$ (530 nm), hexane (550 nm), and acetonitrile (560 nm). It is believed that **INDT-NDT** adopts a folded conformation in all solvents, which accounts for its very similar emissions in different solvents. The tightness of the folded structure (pitch length) however depends on the strength of the interactions between solvent molecules and PAH chromophores, thus may be different in different solvents, which explains the small variation of λ_{max}^{fl} in different solvents. **INDT-BT**, however, adopts either a folded conformation (good solvents) or interchain aggregation (poor solvents), leading to two distinct well-separated emissions.

Concentration-dependent absorption (Figures S9−S11) and emission (Figure 4) spectroscopic studies of three polymers in chloroform solutions were also carried out. As shown in Figure 4, **INDT-TT** shows two distinct types of emissions: vibronically resolved emissions at 510 and 540 nm in dilute solutions and a broad featureless emission at ∼590 nm in concentrated solutions. Consistent with solvent-dependent studies, the former is interpreted as emissions from random coil, whereas the broad featureless emission is due to interchain aggregates at high concentrations. **INDT-NDT** polymer shows nearly the same broad featureless emission with only a slight blueshift in emission λ_{max} during dilution, indicating that **INDT-NDT** polymer maintains the folding conformation in all chloroform solutions. Note that the narrowness of the emission peak for relatively concentrated solutions is due to the self-absorption of **INDT-NDT** as a result of its small Stokes shift. For **INDT-BT**, however, the emission λ_{max} (640 nm) decreases continuously initially, then reaches and stays at ∼560 nm during further dilutions. The emission at 560 nm is broad and featureless. Again, consistent with solvent-dependent studies, the 560 nm emission is due to a folding conformation, whereas the 640 nm emission is due to interchain aggregation.

Although the above interpretations are logical, direct evidence is needed to support the persistent folding hypothesis of **INDT-NDT**. Folded helices are chiral, and if one handedness can be made dominant, then CD signals can be detected that can serve as the direct evidence for helical folding.[42-44] We thus carried out CD studies on all three polymers. As expected for an achiral molecule or a racemic mixture, neither **INDT-TT** nor **INDT-BT** shows discernible CD signals (Figure 5a) in a dilute THF solution. Surprisingly and to our delight, the **INDT-NDT** solution exhibits distinct positive CD signals in the wavelength range where **INDT-NDT** absorbs (Figure 5a), implying the existence of a helical bias in **INDT-NDT**, or in other words, the dominance of one
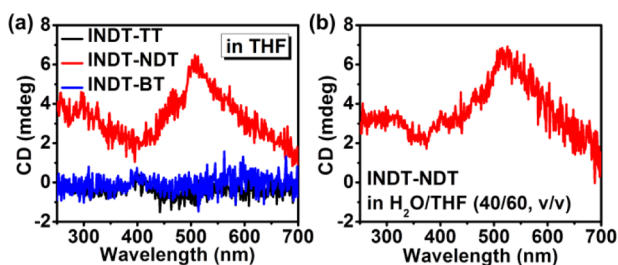
Figure 5. (a) CD spectra of three INDT-containing conjugated polymers measured in THF solutions at 298 K. The absorbance maxima of the solutions were approximately 1.0. (b) CD spectra of **INDT-NDT** (0.085 mM) measured in a mixed solvent of 40% water in THF (by volume) at 298 K.

Figure 6. Cyclic voltammograms of polymer thin films.

particular helix (*P* or *M*) over the other (*M* or *P*). (Note that the alkylating agents used for the synthesis of monomers **1** and **2** are racemic and that the branched alkyl chains have no visible absorption.) This is surprising because one would expect a racemic mixture to be formed during folding because there is no bias favoring either left- or right-handed helices. We noticed that the **INDT-NDT** particles collected after precipitation are highly crystalline. It is likely that **INDT-NDT** foldamers with the same handedness are preferentially aggregated during solution concentration and precipitation processes, making **INDT-NDT** particles with one handed helix dominant over the other. When such a particle is picked and dissolved for CD studies, CD signals can be observed. Although this deserves further studies, the fact that clear CD signals are observed in **INDT-NDT** solutions confirms that **INDT-NDT** does form helical foldamers.

In a H₂O/THF (40:60) solvent mixture, **INDT-NDT** showed positive CD signals with intensity comparable to that in THF (Figure 5b). This supports the notion that **INDT-NDT** chains fold in both good and poor solvents. It is worth noting that the major peak in CD spectrum red-shifted from ∼508 nm in THF to ∼524 nm in the mixed solvent. This is consistent with the observed red-shifted absorption tail (Figure S12) and fluorescence emission spectra in poor solvents as a result of stronger intrachain π−π stacking forces. In this poor solvent, **INDT-NDT** helical structures tend to aggregate presumably through alkyl chain interdigitation to form particles of large size as revealed by particle size analysis. (The measured effective diameter is 885.85 nm with a polydispersity of 0.266.)

The electrochemical properties of the three INDT-containing conjugated polymers were investigated as thin films using CV measurements. As shown in Figure 6, polymers **INDT-TT** and **INDT-BT** show two reversible or semireversible reduction waves during the cathodic scan and two irreversible oxidation waves in the anodic scan. Polymer **INDT-NDT** however shows one semireversible reduction wave and two irreversible oxidation waves in the cathodic and anodic scans, respectively. From the first oxidation onset potential in the anodic scan and the first reduction onset potential in the cathodic scan, the HOMO/LUMO energy levels of the polymers were calculated to be −5.29/−2.93, −5.45/−2.42, and −5.57/−3.41 eV (Table 2) for **INDT-TT**, **INDT-NDT**, and **INDT-BT**, respectively. Their bandgaps are determined to be 2.36, 3.03, and 2.16 eV, respectively, generally higher than those calculated from their absorption onsets. The higher estimates from CV measurements may be due to the interface barrier between the polymer and the electrode surface as shown in other polymer systems.[45]
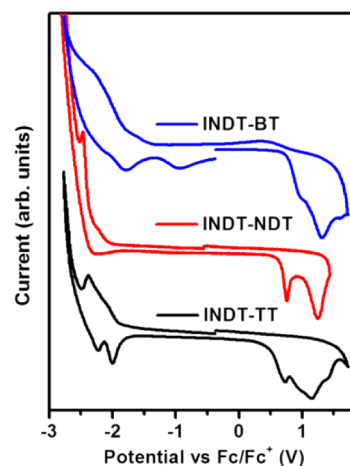
Charge carrier (hole in this case) mobility of as-spin-coated and thermally annealed thin films of the polymers were measured by the steady-state SCLC technique. Hole-only devices were fabricated with the configuration of ITO/PEDOT:PSS/polymer/MoO₃/Au, as illustrated in Figure 7a. The active area of individual devices is 0.14 cm², typical of organic solar cells, which is defined by the overlap area of ITO and the deposited MoO₃/Au electrodes. The contacts are assumed to be ohmic on the basis of the energy levels (Figure 7b) of the polymers and the employed electron-blocking layers (PEDOT:PSS and MoO₃).

The active layers (polymer thin films) were deposited by spin-coating of ODCB solutions, followed by solvent annealing. The spin-coated films have a thickness of 120−620 nm. Figure 8 shows their UV−vis absorption spectra before and after thermal annealing. Compared to the corresponding absorption spectra in dilute chloroform solutions (Figure 2), the film absorption of **INDT-NDT** shows minimal shift in absorption wavelengths and band edge, except for a clear tail extending beyond 800 nm. The shape of the tail indicates that it may be due to light scattering (diffraction) instead of absorption. Significant changes however are observed for the absorption spectra of **INDT-TT** and **INDT-BT** films. For **INDT-TT**, although the absorption λ_{max} of its film is about the same as that of its solution, a clear new shoulder band in the long wavelength range from 550 to 700 nm was observed in its film absorption spectrum. The absorption in the same long wavelength range is also significantly enhanced in the film absorption spectrum of **INDT-BT**, so much so that the absorbance at 560 nm is as strong as that at 530 nm and the absorption band edge is red-shifted by more than 20 nm. These results indicate that **INDT-NDT** may maintain the same conformation in both solution and film, whereas **INDT-TT** and **INDT-BT** change conformations. The observation of significantly red-shifted absorption and significantly red-shifted structureless emission (Figure S13) of **INDT-TT** and **INDT-BT** films indicates that both polymers exist as interchain aggregates with strong backbone π−π stacking interactions. Note that in dilute chloroform solutions, **INDT-TT** chains are monomeric random coils, whereas **INDT-BT** chains are foldamers. Figure 8 also shows that thermal annealing of these polymer thin films at 120 °C for 10 min results in no changes in their absorption spectra.

Table 2. Experimental and Calculated Frontier Energy Levels and SCLC Hole Mobilities of the Polymers

polymer	experimental[a]			calculated[b]			μ_h (cm^2 V^{-1} s^{-1})	
	E_{HOMO} (eV)	E_{LUMO} (eV)	E_g (eV)	E_{HOMO} (eV)	E_{LUMO} (eV)	E_g (eV)	pristine film[c]	blend BHJ film[c,d]
INDT-TT	−5.29	−2.93	2.36	−5.44	−2.64	2.80	2.20×10^{-6} (2.36×10^{-6})	9.18×10^{-3} (5.88×10^{-3})
INDT-NDT	−5.45	−2.42	3.03	−5.36	−2.39	2.97	2.77×10^{-2} (1.25×10^{-2})	1.29×10^{-1} (9.97×10^{-2})
INDT-BT	−5.57	−3.41	2.16	−5.66	−3.16	2.60	8.79×10^{-5} (1.37×10^{-3})	2.66×10^{-4} (2.09×10^{-4})

[a]From CV measurement of thin solid film. [b]Using DFT calculations at the B3LYP/6-31G(d) level for the dimers shown in Figure 1. [c]Value in parentheses is the SCLC mobility of thin film thermally annealed at 120 °C for 10 min. [d]Polymer:PC$_{71}$BM (1:1, w/w).
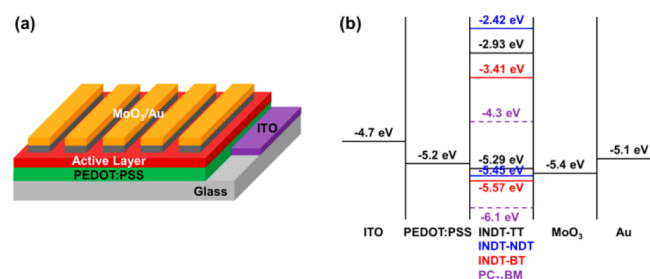

Figure 7. (a) Structure of hole-only devices. (b) Energy level diagram showing the HOMO and LUMO energies of each of the materials used in the devices.
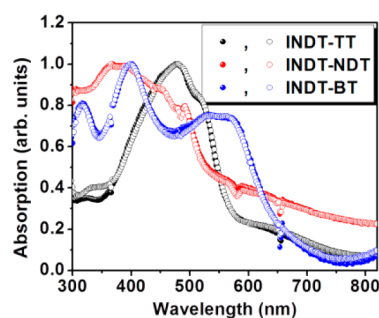

Figure 8. Absorption spectra of polymer thin films before (filled circles) and after (empty circles) thermal annealing (at 120 °C for 10 min) under nitrogen atmosphere.

Figure 9 displays the AFM topography images of these polymer thin films before and after thermal annealing. The pristine thin films of **INDT-TT** and **INDT-BT** polymers both show a rather uniform surface with root-mean-square (RMS) roughness of only 1.77 and 1.06 nm, respectively, whereas that
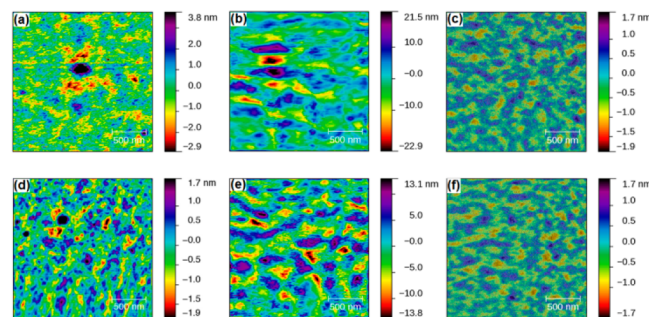

Figure 9. AFM topography images of thin films of **INDT-TT** (a and d), **INDT-NDT** (b and e), and **INDT-BT** (c and f), before (a–c) and after (d–f) thermal annealing at 120 °C for 10 min under nitrogen atmosphere.

of **INDT-NDT** polymer is a relatively rough one with RMS roughness of 9.31 nm. This is likely due to the foldamer structure of **INDT-NDT** polymer: some folding helices lay flat, whereas others may stand up, creating the surface roughness. Thermal annealing reduced the surface roughness for **INDT-TT** (with RMS roughness of 0.91 nm) and **INDT-NDT** (with RMS roughness of 7.37 nm) films but exerted little effect on the INDT-BT film. In light of their film thickness (**INDT-TT** ≈ 120 nm; **INDT-NDT** ≈ 620 nm; **INDT-BT** ≈ 420 nm), the surface roughness for all three polymers can be considered small and acceptable for SCLC measurements.

The $J-V$ characteristics of the hole-only devices of the pristine and thermally annealed thin films of the three polymers are depicted in Figure 10a–c. The hole mobilities of the polymer thin films were obtained by fitting these $J-V$ curves in the SCLC region using the following equation[12]

$$J = \frac{9}{8}\varepsilon_0\varepsilon_r\mu\frac{(V_{app} - V_{bi})^2}{d^3}$$

where J is the current density in the SCLC region, V_{app} is the applied voltage, V_{bi} is the built-in voltage, ε_0 is the permittivity of free space (8.854×10^{-12} F m^{-1}), ε_r is the relative dielectric constant of the thin film that is assumed to be 3 (a typical value for an organic semiconductor),[12] μ is the charge carrier mobility, and d is the film thickness. The derived SCLC hole mobility values are summarized in Table 2.

The pristine thin films of **INDT-TT** and **INDT-BT** polymers exhibit a hole mobility of 2.20×10^{-6} and 8.79×10^{-5} cm^2 V^{-1} s^{-1}, respectively, both of which are typical for spin-coated thin films of conjugated polymers whose SCLC hole mobility usually falls in the range of 10^{-6} to $\sim 10^{-3}$ cm^2 V^{-1} s^{-1}.[8,12–14] In contrast, a very high SCLC hole mobility, up to 2.77×10^{-2} cm^2 V^{-1} s^{-1}, was observed for the pristine thin film of **INDT-NDT** polymer. This value is among the highest reported SCLC hole mobilities for solution-processed conjugated polymers.[15,16]

With the above SCLC hole mobilities in the pristine thin films of three polymers, it would be interesting to investigate further their performance in polymer:fullerene blend films. Therefore, referring to the energy level diagram of the materials as shown in Figure 7b, we fabricated hole-only devices and studied the SCLC hole mobility of these polymers in polymer:PC$_{71}$BM (1:1, w/w) blend films. The introduction of PC$_{71}$BM into the thin solid film is found to increase the SCLC hole mobility for all three INDT-containing polymers but to different extents (Figure 10d–f and Table 2). The blend thin film of **INDT-TT**:PC$_{71}$BM exhibits a relatively high SCLC hole mobility of 9.18×10^{-3} cm^2 V^{-1} s^{-1}, which is more than three orders of magnitude higher than that of the **INDT-TT** pristine thin film (2.20×10^{-6} cm^2 V^{-1} s^{-1}). The hole mobility of the blend thin films of **INDT-NDT**:PC$_{71}$BM and **INDT-**
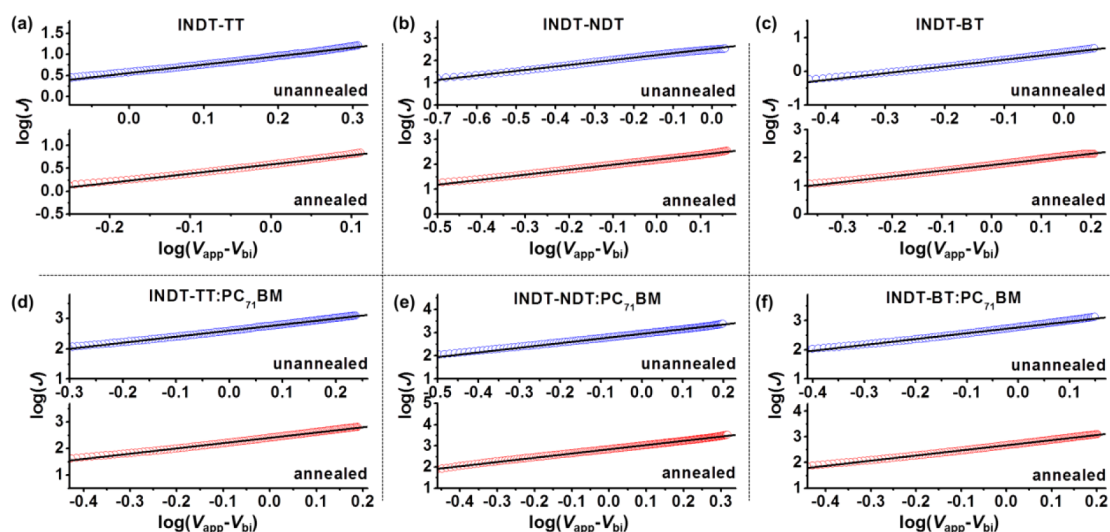
Figure 10. Experimental (empty circles) and fitted (black lines) current density−voltage characteristics of ITO/PEDOT:PSS/active layer/MoO$_3$/Au devices with the active layer being **INDT-TT** (a), **INDT-NDT** (b), **INDT-BT** (c), or their blends with PC$_{71}$BM (1:1, w/w) (d−f), before (blue) or after (red) thermal annealing (at 120 °C for 10 min).
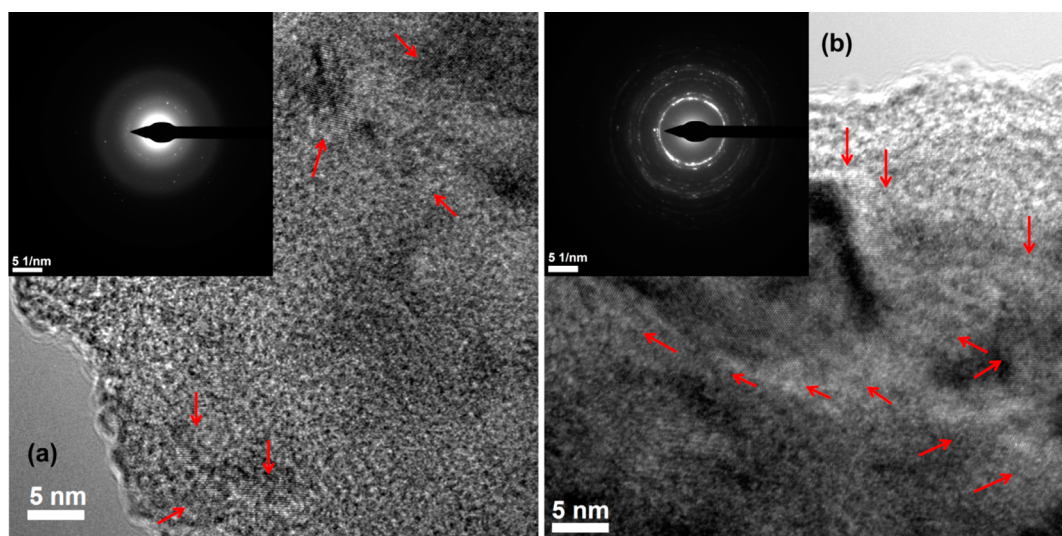

Figure 11. HRTEM images of **INDT-NDT** pristine polymer thin film (a) and **INDT-NDT**:PC$_{71}$BM (1:1, w/w) blend thin film (b). Insets show their corresponding FFT electron diffraction patterns. Red arrows indicate the lattice fringes. For more HRTEM images, please see Figures S15 and S18 in the Supporting Information.

BT:PC$_{71}$BM is increased by a factor of ∼4.6 to a remarkably high value of 1.29×10^{-1} cm^2 V^{-1} s^{-1} and by a factor of ∼3.0 to 2.66×10^{-4} cm^2 V^{-1} s^{-1}, respectively, as compared to that of the corresponding pristine polymer thin films. To our knowledge, 1.29×10^{-1} cm^2 V^{-1} s^{-1} is the highest-ever reported SCLC hole mobility for solution-processed conjugated polymer:fullerene blends.[15,16]

To understand the origin of the high SCLC hole mobility of **INDT-NDT**, thin films of pure polymers and polymer:PC$_{71}$BM blends were subjected to HRTEM (Figures 11, 12, and S14−S19) and XRD (Figure 13) studies. Although the HRTEM images of **INDT-TT** and **INDT-BT** (Figures S14 and S16) reveal no crystalline order, **INDT-NDT** films show clear crystalline domains with distinct crystalline lattice fringes (Figure 11a). The size of the nanocrystalline domains varies from several to a couple of tens of nanometers, and the lattice fringe spacing is ∼0.212 nm. The fast Fourier-transformed (FFT) electron diffraction pattern of the pristine **INDT-NDT**

thin film (inset, Figure 11a) shows spot rings that clearly indicate the nanocrystalline nature of the film.

The XRD diffractogram of **INDT-NDT** pristine thin film (Figure 13) shows a narrow peak centered at ∼7.2° (d spacing = 12.3 Å) with relatively high intensity and a broad weak peak centered at ∼15.2° (d spacing = 5.8 Å), whereas those of **INDT-TT** and **INDT-BT** pristine thin films (Figure 13) display only very weak broad peaks (at ∼19.8° (d spacing = 4.5 Å) and ∼25.3° (d spacing = 3.5 Å) for **INDT-TT**; at ∼18.9° (d spacing = 4.7 Å) and ∼25.7° (d spacing = 3.5 Å) for **INDT-BT**), confirming the existence of crystalline order in **INDT-NDT** film and the amorphous nature of **INDT-TT** and **INDT-BT** films. The regular d spacing of 3.5 Å observed for **INDT-TT** and **INDT-BT** corresponds to the interchain π−π stacking (in the typical range of 3.3−3.8 Å).[46−48] This d spacing is absent in **INDT-NDT**. The d spacing of 4.5 and 4.7 Å for **INDT-TT** and **INDT-BT**, respectively, can be viewed as an intrachain π−π stacking distance.[49] The d spacing of 5.8 and
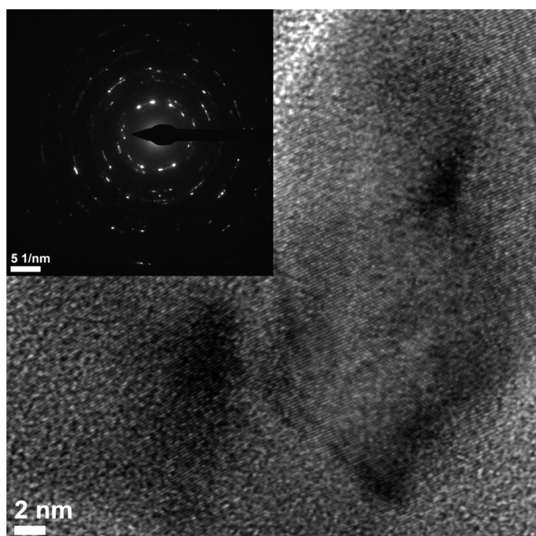
Figure 12. HRTEM image of **INDT-TT**:$PC_{71}BM$ (1:1, w/w) blend thin film. The inset shows its FFT electron diffraction pattern. Please see the Supporting Information for more HRTEM images.
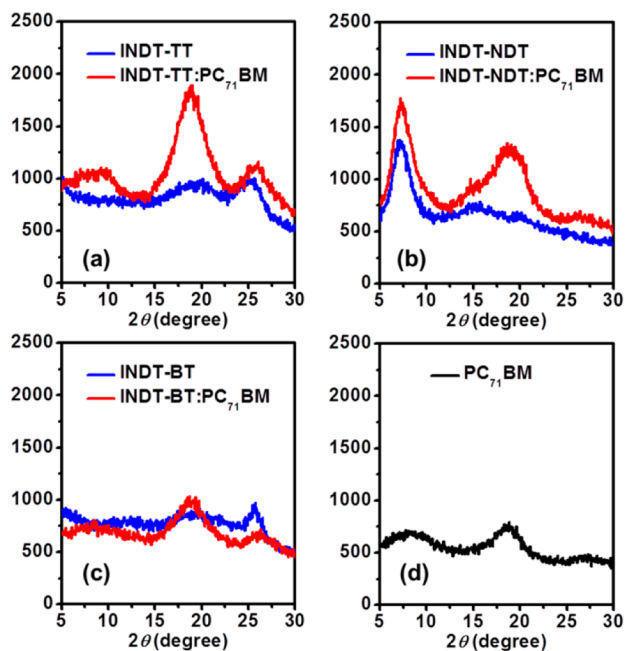
Figure 13. XRD patterns of thin films of **INDT-TT** and **INDT-TT**:$PC_{71}BM$ (a), **INDT-NDT** and **INDT-NDT**:$PC_{71}BM$ (b), **INDT-BT** and **INDT-BT**:$PC_{71}BM$ (c), and $PC_{71}BM$ fabricated on Si zero-diffraction plates (d). Labels for all *y* axes (i.e., counts) are omitted.

12.3 Å, unique to **INDT-NDT**, must be exclusively associated with its helical folding structures. Referring to a simulated geometry of **INDT-NDT** helical foldamer (Figure S21 and related discussion in the Supporting Information), the *d* spacing of 5.8 Å can be assigned to the thread pitch ($\pi-\pi$ stacking within a folded helix), whereas the *d* spacing of 12.3 Å can be reasonably treated as interhelix spacing distance because it matches well with the length of its surrounding alkyl chains. To obtain a helical folding model for **INDT-NDT**, theoretical calculations were performed in gas phase using the HF/3-21G method. A hexamer in a folding structure as shown in Figure S8b was taken as the starting point for calculation. To minimize the computational efforts, the 2-butyloctyl chains at the imide

position of INDTs and the dodecyloxy chains in the NDT units were truncated to methyl and methoxy groups, respectively. Without considering $\pi-\pi$ stacking, the energy-minimized helical model (Figure S20) has a dihedral angle of ~41.8° between the adjacent INDT and NDT units and a thread pitch around 10 Å. To obtain a helical model that closely matches the XRD results (thread pitch ≈ 5.8 Å), we have sought to adjust the dihedral angle. It was found that the foldamer model has a thread pitch of 5.8 Å when the dihedral angle is ~13° (Figure S21). This dihedral angle is very close to that obtained by DFT calculations as previously discussed (Figure 1b). Such a folding structure is highly ordered with clear $\pi-\pi$ overlaps between stacked PAH units. The strong $\pi-\pi$ interaction is likely the driving force for the foldamer formation.

Although **INDT-TT** pristine thin films show no crystallinity, the **INDT-TT**:$PC_{71}BM$ blend film displays surprisingly high crystallinity, evident from its HRTEM image and XRD pattern. As shown in Figure 12, domains of distinct crystalline lattice fringes with a size of several tens of nanometers and lattice fringe spacing of ~0.201 nm were observed. The FFT electron diffraction pattern of the blend film (inset of Figure 12) confirmed the high nanocrystallinity of the **INDT-TT**:$PC_{71}BM$ blend film. This crystallinity change is also reflected in its XRD diffractogram, which shows clearly the appearance of a new broad peak centered at ~9.2° and the increase in intensity of peaks centered at ~18.8 and ~26.0° where the contribution from the ordering of $PC_{71}BM$ cannot be ignored. A pure $PC_{71}BM$ pristine thin film prepared under the same conditions (Figure 13d) shows only two broad and weak peaks centered at 8.3 and ~18.8°.

Blending **INDT-NDT** with $PC_{71}BM$ leads to further enhanced crystallinity in its films as well. As seen from the HRTEM images (Figures 11a,b), the domains of distinct crystalline lattice fringes change from isolated sporadic domains in the **INDT-NDT** pristine film to widespread in the **INDT-NDT**:$PC_{71}BM$ blend film. The FFT electron diffraction pattern of the blend film (Figure 11b) showed more clear dotted rings. Consistent with the HRTEM results, the XRD of the **INDT-NDT**:$PC_{71}BM$ blend film displayed bands with increased intensities.

The emerging crystallinity of **INDT-TT**:$PC_{71}BM$ blend film and the improved crystallinity of **INDT-NDT**:$PC_{71}BM$ blend film must come from a synergetic effect of the polymers and $PC_{71}BM$. The enhanced crystalline order is most likely responsible for the increase of their charge carrier mobilities.

For the **INDT-BT**:$PC_{71}BM$ blend film, however, no crystalline order was observed in its HRTEM image (Figure S19). Its XRD diffractogram (Figure 13) is merely a simple superposition of those of **INDT-BT** polymer and $PC_{71}BM$ thin films. This is consistent with its low mobility.

The hole mobilities of **INDT-TT** and **INDT-NDT** thin films are slightly lower after thermal annealing, 2.36×10^{-6} and 1.25×10^{-2} cm² V⁻¹ s⁻¹, respectively, whereas that of **INDT-BT** is increased (from 8.79×10^{-5} to 1.37×10^{-3} cm² V⁻¹ s⁻¹). Thermal annealing led to slightly decreased hole mobility for all three polymer:$PC_{71}BM$ blends as well. (The hole mobility of the **INDT-TT**:$PC_{71}BM$, **INDT-NDT**:$PC_{71}BM$ and **INDT-BT**:$PC_{71}BM$ blend films is 5.88×10^{-3}, 9.97×10^{-2} and 2.09×10^{-4} cm² V⁻¹ s⁻¹, respectively after thermal annealing.) Consistent with the findings from our previously reported INDT-containing conjugated polymers, the thermal annealing process is not a necessity for the fabrication of their thin films from a propertywise perspective.

The HRTEM and XRD studies show a clear correlation between hole mobility and film crystallinity. It is remarkable that both polymers **INDT-NDT** and **INDT-BT** are found to adopt a folded conformation in good solvents and share the same INDT monomer yet show mobility values differing by nearly 3 orders of magnitude. As discussed earlier, although **INDT-BT** adopts a folded conformation in dilute solutions of good solvents, interchain aggregates dominate in poor solvents. The strong interchain stacking interaction is presumably due to its flat backbone. In a concentrated solution of good solvent, such as the one for thin film preparation, most polymer chains of **INDT-BT** may favor interchain aggregation, instead of the folding conformation, which is supported by the dilution experiments (Figures 4 and S11) and the film emission studies (Figure S13) where only aggregate emission is observed. **INDT-NDT**, however, adopts a folded conformation in both good and poor solvents. Two factors may contribute to **INDT-NDT**'s preference of folding over interchain aggregation: One is the strong $\pi-\pi$ stacking interaction in the folded conformation because of the PAH-only backbone components, and the other is the sizable twist between the INDT and NDT units that hampers interchain aggregation. On the basis of the dilution experiments (Figures 4 and S10) and thin film emission studies (Figure S13), it is reasonable to assume that **INDT-NDT** polymers maintain a folded conformation in concentrated ODCB solutions and in spin-coated films. As discussed earlier, HRTEM images clearly show that **INDT-NDT** films contain nanocrystalline domains, whereas **INDT-TT** and **INDT-BT** do not (Figures 11 and S14−S16). X-ray studies (Figure 13) show that **INDT-NDT** films show long-range order (d spacing = 12.3 and 5.8 Å), which is missing in **INDT-TT** and **INDT-BT** films. The 12.3 Å d spacing can be assigned to the separation distance of adjacent foldamers dictated by the dodecyl chain interdigitation, whereas the 5.8 Å d spacing is the thread pitch of helices. The high crystallinity of **INDT-NDT** appears to be associated with the high folding propensity of **INDT-NDT** polymers. Folded helices, unlike random stretched chains, are more ordered structures themselves (Figure S21). Moreover, folding limits backbone flexibility and extends alkyl chains outward, which is conducive to chain interdigitation and thus the helices' organization. Therefore, the folded helices are easily organized into larger ordered domains. Because the folding of an **INDT-NDT** polymer chain results in stacked hole-transporting PAH columns that are conductive to charge transport, high mobility of **INDT-NDT** films can thus be understood.

CONCLUSIONS

We have synthesized three discotic conjugated polymers, **INDT-TT**, **INDT-NDT**, and **INDT-BT**, with INDT as the monomer unit and TT, NDT, and BT, respectively, as the comonomer unit in the backbone and studied their optical, electrochemical, crystalline properties, and SCLC hole mobilities. DFT calculations reveal that **INDT-BT** has a planar backbone geometry, whereas **INDT-TT** and **INDT-BT** are somewhat twisted. Optical studies indicate that the three polymers adopt very different conformations in solutions. In a dilute solution of a good solvent, **INDT-TT** is random stretched monomeric chains, whereas **INDT-NDT** and **INDT-BT** are foldamers. In poor solvents or concentrated solutions of good solvents, both **INDT-TT** and **INDT-BT** form interchain aggregates, whereas **INDT-NDT** maintains the folded conformation. The helical folding of the **INDT-NDT**

polymer in solutions was confirmed by CD spectroscopic studies. Spin-coated and subsequently solvent-annealed thin films of the three polymers show SCLC hole mobility of 2.20×10^{-6}, 2.77×10^{-2}, and 8.79×10^{-5} cm^2 V^{-1} s^{-1} for **INDT-TT**, **INDT-NDT**, and **INDT-BT**, respectively. The very high SCLC hole mobility of **INDT-NDT** thin films was attributed to its high nanocrystallinity, which was confirmed by HRTEM and powder XRD measurements. Blending the polymer with PC$_{71}$BM was found to increase the crystallinity of **INDT-NDT**, which was accompanied by further increased hole mobilities. The spin-coated film of **INDT-NDT**:PC$_{71}$BM blend showed an SCLC hole mobility of 1.29×10^{-1} cm^2 V^{-1} s^{-1}, representing one of the highest mobility values ever reported on solution-processed organic semiconducting thin films. Thermal annealing of the thin films, in most cases, shows a negligible or detrimental effect on hole mobility. The persistent folded conformation of **INDT-NDT** is believed to be responsible for the high crystallinity of its thin films and its high SCLC mobilities. It is expected that these findings will help guide the rational design of new conjugated polymers with even higher charge mobilities.

ASSOCIATED CONTENT

Ⓢ Supporting Information

Preparation of **2−4**; ^{1}H NMR spectra, fluorescence emission and excitation spectra of **INDT-TT** in dilute CHCl$_3$ solution; envisioned foldamer formation of **INDT-BT** and **INDT-NDT** polymers; changes in UV−vis absorption spectra of CHCl$_3$ solutions of three polymers upon continuous dilution; fluorescence emission spectra of polymer thin films; HRTEM images of the pristine polymer thin films and polymer:PC$_{71}$BM (1:1, w/w) blend thin films; energy-minimized geometry of an **INDT-NDT** oligomer calculated with the HF/3-21G method; molecular model of **INDT-NDT** helical foldamers; AFM topographic and phase images of **INDT-NDT** and **INDT-NDT**:PC$_{71}$BM (1:1, w/w) thin films; and photovoltaic properties of the polymer:PC$_{71}$BM (1:1, w/w) blend thin films. The Supporting Information is available free of charge on the ACS Publications website at DOI: 10.1021/acsami.5b01676.

AUTHOR INFORMATION

Corresponding Author

*E-mail: pengz@umkc.edu.

Notes

The authors declare no competing financial interest.

ACKNOWLEDGMENTS

ABBREVIATIONS

NMR, nuclear magnetic resonance; HRTEM, high-resolution transmission electron microscopy; rpm, rotations per minute; XRD, X-ray diffraction

■ REFERENCES

(1) Sundar, V. C.; Zaumseil, J.; Podzorov, V.; Menard, E.; Willett, R. L.; Someya, T.; Gershenson, M. E.; Rogers, J. A. Elastomeric Transistor Stamps: Reversible Probing of Charge Transport in Organic Crystals. *Science* **2004**, *303*, 1644−1646.

(2) Günes, S.; Neugebauer, H.; Sariciftci, N. S. Conjugated Polymer-Based Organic Solar Cells. *Chem. Rev.* **2007**, *107*, 1324−1338.

(3) García-Frutos, E. M.; Pandey, U. K.; Termine, R.; Omenat, A.; Barberá, J.; Serrano, J. L.; Golemme, A.; Gómez-Lor, B. High Charge Mobility in Discotic Liquid-Crystalline Triindoles: Just a Core Business? *Angew. Chem., Int. Ed.* **2011**, *50*, 7399−7402.

(4) Heeger, A. J. 25th Anniversary Article: Bulk Heterojunction Solar Cells: Understanding the Mechanism of Operation. *Adv. Mater.* **2014**, *26*, 10−28.

(5) van Duren, J. K. J.; Yang, X.; Loos, J.; Bulle-Lieuwma, C. W. T.; Sieval, A. B.; Hummelen, J. C.; Janssen, R. A. J. Relating the Morphology of Poly(*p*-phenylene vinylene)/Methanofullerene Blends to Solar-Cell Performance. *Adv. Funct. Mater.* **2004**, *14*, 425−434.

(6) Hoppe, H.; Niggemann, M.; Winder, C.; Kraut, J.; Hiesgen, R.; Hinsch, A.; Meissner, D.; Sariciftci, N. S. Nanoscale Morphology of Conjugated Polymer/Fullerene-Based Bulk-Heterojunction Solar Cells. *Adv. Funct. Mater.* **2004**, *14*, 1005−1011.

(7) Xie, W.; McGarry, K. A.; Liu, F.; Wu, Y.; Ruden, P. P.; Douglas, C. J.; Frisbie, C. D. High-Mobility Transistors Based on Single Crystals of Isotopically Substituted Rubrene-d_{28}. *J. Phys. Chem. C* **2013**, *117*, 11522−11529.

(8) Thompson, B. C.; Kim, B. J.; Kavulak, D. F.; Sivula, K.; Mauldin, C.; Fréchet, J. M. J. Influence of Alkyl Substitution Pattern in Thiophene Copolymers on Composite Fullerene Solar Cell Performance. *Macromolecules* **2007**, *40*, 7425−7428.

(9) Li, Y.; Clevenger, R. G.; Jin, L.; Kilway, K. V.; Peng, Z. Unusually High SCLC Hole Mobility in Solution-Processed Thin Films of a Polycyclic Thiophene-Based Small-Molecule Semiconductor. *J. Mater. Chem. C* **2014**, *2*, 7180−7183.

(10) Sirringhaus, H.; Brown, P. J.; Friend, R. H.; Nielsen, M. M.; Bechgaard, K.; Langeveld-Voss, B. M. W.; Spiering, A. J. H.; Janssen, R. A. J.; Meijer, E. W.; Herwig, P.; de Leeuw, D. M. Two-Dimensional Charge Transport in Self-Organized, High-Mobility Conjugated Polymers. *Nature* **1999**, *401*, 685−688.

(11) Kang, I.; Yun, H.-J.; Chung, D. S.; Kwon, S.-K.; Kim, Y.-H. Record High Hole Mobility in Polymer Semiconductors via Side-Chain Engineering. *J. Am. Chem. Soc.* **2013**, *135*, 14896−14899.

(12) Zhang, L.; Xing, X.; Chen, Z.; Xiao, L.; Qu, B.; Gong, Q. Highly Efficient Polymer Solar Cells by using the Homogeneous Self-Assembly of a Sulphydryl-Capped Photoactive Polymer Covalently Bound to the Anode. *Energy Technol.* **2013**, *1*, 613−616.

(13) Guo, X.; Zhou, N.; Lou, S. J.; Smith, J.; Tice, D. B.; Hennek, J. W.; Ortiz, R. P.; Navarrete, J. T. L.; Li, S.; Strzalka, J.; Chen, L. X.; Chang, R. P. H.; Facchetti, A.; Marks, T. J. Polymer Solar Cells with Enhanced Fill Factors. *Nat. Photonics* **2013**, *7*, 825−833.

(14) Ng, A.; Liu, X.; Jim, W. Y.; Djurišić, A. B.; Lo, K. C.; Li, S. Y.; Chan, W. K. P3HT: PCBM Solar Cells—The Choice of Source Material. *J. Appl. Polym. Sci.* **2014**, *131*, 1−9.

(15) Murphy, L.; Hong, W.; Aziz, H.; Li, Y. Organic Photovoltaics with Thick Active Layers (∼800 nm) Using a High Mobility Polymer Donor. *Sol. Energy Mater. Sol. Cells* **2013**, *114*, 71−81.

(16) Murphy, L.; Hong, W.; Aziz, H.; Li, Y. Influences of Using a High Mobility Donor Polymer on Solar Cell Performance. *Org. Electron.* **2013**, *14*, 3484−3492.

(17) Zhang, M.; Gu, Y.; Guo, X.; Liu, F.; Zhang, S.; Huo, L.; Russell, T. P.; Hou, J. Efficient Polymer Solar Cells Based on Benzothiadiazole and Alkylphenyl Substituted Benzodithiophene with a Power Conversion Efficiency over 8%. *Adv. Mater.* **2013**, *25*, 4944−4949.

(18) Liang, Y.; Xu, Z.; Xia, J.; Tsai, S.-T.; Wu, Y.; Li, G.; Ray, C.; Yu, L. For the Bright Future—Bulk Heterojunction Polymer Solar Cells with Power Conversion Efficiency of 7.4%. *Adv. Mater.* **2010**, *22*, E135−E138.

(19) He, Z.; Zhong, C.; Huang, X.; Wong, W.-Y.; Wu, H.; Chen, L.; Su, S.; Cao, Y. Simultaneous Enhancement of Open-Circuit Voltage, Short-Circuit Current Density, and Fill Factor in Polymer Solar Cells. *Adv. Mater.* **2011**, *23*, 4636−4643.

(20) Peng, Q.; Huang, Q.; Hou, X.; Chang, P.; Xu, J.; Deng, S. Enhanced Solar Cell Performance by Replacing Benzodithiophene with Naphthodithiophene in Diketopyrrolopyrrole-Based Copolymers. *Chem. Commun.* **2012**, *48*, 11452−11454.

(21) Badgujar, S.; Song, C. E.; Shin, W. S.; Moon, S.-J.; Kang, I.-N.; Lee, J.; Cho, S.; Lee, S. K.; Lee, J.-C. Synthesis and Characterization of a Novel Naphthodithiophene-Based Copolymer for Use in Polymer Solar Cells. *Macromolecules* **2012**, *45*, 6938−6945.

(22) Uy, R. L.; Price, S. C.; You, W. Structure-Property Optimizations in Donor Polymers via Electronics, Substituents, and Side Chains Toward High Efficiency Solar Cells. *Macromol. Rapid Commun.* **2012**, *33*, 1162−1177.

(23) Zhou, H.; Yang, L.; Price, S. C.; Knight, K. J.; You, W. Enhanced Photovoltaic Performance of Low-Bandgap Polymers with Deep LUMO Levels. *Angew. Chem., Int. Ed.* **2010**, *49*, 7992−7995.

(24) Zhao, X.; Yang, D.; Lv, H.; Yin, L.; Yang, X. New Benzotrithiophene Derivative with a Broad Band Gap for High Performance Polymer Solar Cells. *Polym. Chem.* **2013**, *4*, 57−60.

(25) Sirringhaus, H.; Friend, R. H.; Wang, C.; Leuninger, J.; Müllen, K. Dibenzothienobisbenzothiophene-A Novel Fused-Ring Oligomer with High Field-Effect Mobility. *J. Mater. Chem.* **1999**, *9*, 2095−2101.

(26) Watson, M. D.; Fechtenkötter, A.; Müllen, K. Big Is Beautiful—"Aromaticity" Revisited from the Viewpoint of Macromolecular and Supramolecular Benzene Chemistry. *Chem. Rev.* **2001**, *101*, 1267−1300.

(27) Schmidt-Mende, L.; Fentenkötter, A.; Müllen, K.; Moons, E.; Friend, R. H.; MacKenzie, J. D. Self-Organized Discotic Liquid Crystals for High-Efficiency Organic Photovoltaics. *Science* **2001**, *293*, 1119−1122.

(28) Wong, W. W. H.; Ma, C.-Q.; Pisula, W.; Yan, C.; Feng, X.; Jones, D. V.; Müllen, K.; Janssen, R. A. J.; Bäuerle, P.; Holmes, A. B. Self-Assembling Thiophene Dendrimers with a Hexa-*peri*-hexabenzocoronene Core−Synthesis, Characterization and Performance in Bulk Heterojunction Solar Cells. *Chem. Mater.* **2010**, *22*, 457−466.

(29) Chou, C.-E.; Li, Y.; Che, Y.; Zang, L.; Peng, Z. Synthesis, Self-Assembly and Photovoltaic Applications of Tribenzopentaphene Derivatives. *RSC Adv.* **2013**, *3*, 20666−20672.

(30) Dutta, T.; Li, Y.; Thornton, A. L.; Zhu, D.-M.; Peng, Z. Imide-Functionalized Naphthodithiophene Based Donor-Acceptor Conjugated Polymers for Solar Cells. *J. Polym. Sci., Part A: Polym. Chem.* **2013**, *51*, 3818−3828.

(31) Li, Y.; Jin, L.; Chakraborty, S.; Li, S.; Lu, P.; Zhu, D.-M.; Yan, X.; Peng, Z. Photovoltaic Properties and Femtosecond Time-Resolved Fluorescence Study of Polyoxometalate-Containing Rod-Coil Diblock Copolymers. *J. Polym. Sci., Part B: Polym. Phys.* **2014**, *52*, 122−133.

(32) Tovar, J. D.; Rose, A.; Swager, T. M. Functionalizable Polycyclic Aromatics through Oxidative Cyclization of Pendant Thiophenes. *J. Am. Chem. Soc.* **2002**, *124*, 7762−7769.

(33) Carsten, B.; He, F.; Son, H. J.; Xu, T.; Yu, L. Stille Polycondensation for Synthesis of Functional Materials. *Chem. Rev.* **2011**, *111*, 1493−1528.

(34) Bujak, P.; Kulszewicz-Bajer, I.; Zagorska, M.; Maurel, V.; Wielgus, I.; Pron, A. Polymers for Electronics and Spintronics. *Chem. Soc. Rev.* **2013**, *42*, 8895−8999.

(35) Frisch, M. J.; Trucks, G. W.; Schlegel, H. B.; Scuseria, G. E.; Robb, M. A.; Cheeseman, J. R.; Montgomery, J. A., Jr.; Vreven, T.; Kudin, K. N.; Burant, J. C.; Millam, J. M.; Iyengar, S. S.; Tomasi, J.; Barone, V.; Mennucci, B.; Cossi, M.; Scalmani, G.; Rega, N.; Petersson, G. A.; Nakatsuji, H.; Hada, M.; Ehara, M.; Toyota, K.; Fukuda, R.; Hasegawa, J.; Ishida, M.; Nakajima, T.; Honda, Y.; Kitao, O.; Nakai, H.; Klene, M.; Li, X.; Knox, J. E.; Hratchian, H. P.; Cross, J. B.; Bakken, V.; Adamo, C.; Jaramillo, J.; Gomperts, R.; Stratmann, R. E.; Yazyev, O.; Austin, A. J.; Cammi, R.; Pomelli, C.; Ochterski, J. W.; Ayala, P. Y.; Morokuma, K.; Voth, G. A.; Salvador, P.; Dannenberg, J. J.; Zakrzewski, V. G.; Dapprich, S.; Daniels, A. D.; Strain, M. C.; Farkas, O.; Malick, D. K.; Rabuck, A. D.; Raghavachari, K.; Foresman, J. B.; Ortiz, J. V.; Cui, Q.; Baboul, A. G.; Clifford, S.; Cioslowski, J.;

Stefanov, B. B.; Liu, G.; Liashenko, A.; Piskorz, P.; Komaromi, I.; Martin, R. L.; Fox, D. J.; Keith, T.; Al-Laham, M. A.; Peng, C. Y.; Nanayakkara, A.; Challacombe, M.; Gill, P. M. W.; Johnson, B.; Chen, W.; Wong, M. W.; Gonzalez, C.; Pople, J. A. *Gaussian 03*, revision C.02; Gaussian, Inc.: Wallingford CT, 2003.

(36) Belletête, M.; Durocher, G.; Hamel, S.; Côté, M.; Wakim, S.; Leclerc, M. A First Principles Calculations and Experimental Study of the Ground- and Excited-State Properties of Ladder Oligo(*p*-aniline)s. *J. Chem. Phys.* **2005**, *122*, 104303.

(37) Belletête, M.; Blouin, N.; Boudreault, P.-L. T.; Leclerc, M.; Durocher, G. Optical and Photophysical Properties of Indolocarbazole Derivatives. *J. Phys. Chem. A* **2006**, *110*, 13696−13704.

(38) Kurashige, Y.; Nakajima, T.; Kurashige, S.; Hirao, K.; Nishikitani, Y. Theoretical Investigation of the Excited States of Coumarin Dyes for Dye-Sensitized Solar Cells. *J. Phys. Chem. A* **2007**, *111*, 5544−5548.

(39) Osuna, R. M.; Ortiz, R. P.; Okamoto, T.; Suzuki, Y.; Yamaguchi, S.; Hernández, V.; Navarrete, J. T. L. Thiophene- and Selenophene-Based Heteroacenes: Combined Quantum Chemical DFT and Spectroscopic Raman and UV−Vis−NIR Study. *J. Phys. Chem. B* **2007**, *111*, 7488−7496.

(40) Blouin, N.; Michaud, A.; Gendron, D.; Wakim, S.; Blair, E.; Neagu-Plesu, R.; Belletête, M.; Durocher, G.; Tao, Y.; Leclerc, M. Toward a Rational Design of Poly(2,7-Carbazole) Derivatives for Solar Cells. *J. Am. Chem. Soc.* **2008**, *130*, 732−742.

(41) Chou, C.-E.; Wang, D.; Bagui, M.; Hsu, J.; Chakraborty, S.; Peng, Z. Syntheses and Optical Properties of Triphenylene-Containing Conjugated Polymers. *J. Lumin.* **2010**, *130*, 986−994.

(42) Hill, D. J.; Mio, M. J.; Prince, R. B.; Hughes, T. S.; Moore, J. S. A Field Guide to Foldamers. *Chem. Rev.* **2001**, *101*, 3893−4011.

(43) Prince, R. B.; Barnes, S. A.; Moore, J. S. Foldamer-Based Molecular Recognition. *J. Am. Chem. Soc.* **2000**, *122*, 2758−2762.

(44) Naidu, V. R.; Kim, M. C.; Suk, J.-m.; Kim, H.-J.; Lee, M.; Sim, E.; Jeong, K.-S. Biased Helical Folding of Chiral Oligoindole Foldamers. *Org. Lett.* **2008**, *10*, 5373−5376.

(45) Egbe, D. A. M.; Nguyen, L. H.; Hoppe, H.; Mühlbacher, D.; Sariciftci, N. S. Side Chain Influence on Electrochemical and Photovoltaic Properties of Yne-Containing Poly(phenylene vinylene)s. *Macromol. Rapid Commun.* **2005**, *26*, 1389−1394.

(46) Liu, J.; Zhang, R.; Sauvé, G.; Kowalewski, T.; McCullough, R. D. Highly Disordered Polymer Field Effect Transistors: *N*-Alkyl Dithieno[3,2-*b*:2′,3′-*d*]pyrrole-Based Copolymers with Surprisingly High Charge Carrier Mobilities. *J. Am. Chem. Soc.* **2008**, *130*, 13167−13176.

(47) Janiak, C. A Critical Account on *π−π* Stacking in Metal Complexes with Aromatic Nitrogen-Containing Ligands. *J. Chem. Soc., Dalton Trans.* **2000**, 3885−3896.

(48) Martinez, C. R.; Iverson, B. L. Rethinking the Term "pi-Stacking. *Chem. Sci.* **2012**, *3*, 2191−2201.

(49) Avasthi, K.; Shukla, L.; Kant, R.; Ravikumar, K. Folded Conformations due to Arene Interactions in Dissymmetric and Symmetric Butylidene-Linker Models Based on Pyrazolo[3,4-*d*]-pyrimidine, Purine and 7-Deazapurine. *Acta Crystallogr.* **2014**, *C70*, 555−561.